Clustering dynamic PET images on the Gaussian distributed sinogram domain

Mustafa E. Kamasak*

Istanbul Technical University, Department of Computer Engineering, 34390 Istanbul, Turkey

ABSTRACT

Segmentation of dynamic PET images is an important preprocessing step for kinetic parameter estimation. The time activity curve (TAC) of individual pixels has very low signal-to-noise ratio (SNR). Therefore, the kinetic parameters estimated from the TAC of an individual pixel may not be accurate, and these estimations may have very high spatial variance. To alleviate this problem, pixels with similar kinetic characteristics are clustered into regions, and TACs of pixels within each region are averaged to increase SNR. It has recently been shown that clustering dynamic PET images in the sinogram domain is better than clustering them in the reconstructed image domain [M.E. Kamasak, B. Bayraktar, Clustering dynamic PET images on the projection domain, IEEE Trans. Nucl. Sci. 54 (3) (June 2007) 496–503.]. In that study, the sinograms are assumed to have Poisson distribution. The clusters and TACs of the clusters are then chosen to maximize the posterior probability of the measured sinograms. Although the raw sinogram data are Poisson distributed, the sinogram data corrected for scatter, randoms, attenuation etc. are not Poisson distributed anymore. In this paper, we describe how to cluster dynamic PET images on the sinogram domain when the sinograms are Gaussian distributed.

© 2008 Elsevier Ireland Ltd. All rights reserved.

1. Introduction

Estimation of kinetic parameters for compartment models generally requires the clustering of pixels into physiologically similar regions. Pixels within each physiologically similar region are expected to have similar time activity curves (TAC). TAC extracted from a group of pixels have higher signal-to-noise ratio (SNR) compared to TAC extracted from a single pixel. Therefore, the accuracy of clustering and the precision of the extracted TAC are critical for accurate kinetic parameter estimation. The clustering is generally performed manually, and the TAC of each region is computed by averaging the TACs of the pixels within the region. However, manual clustering is a time-consuming and operator dependent task. It is also challenging because of noise and partial volume effect in

PET images. Automatic clustering algorithms have improved reproducibility, and they are relatively faster compared to manual clustering.

Recently, there has been increasing interest in automatic clustering algorithms for dynamic PET. A modified mixture model algorithm was proposed by Ashburner et al. [2]. This algorithm maximizes the likelihood of a pixel belonging to a cluster given the pixel's TAC. Wong et al. [3] proposed a distance-based clustering algorithm. In that study, pixels are assigned to clusters based on their TACs' weighted distance to the cluster TACs. This algorithm is used for comparison against the method that is proposed in this study, and it is further described in Section 3.1. An expectation maximization (EM) based algorithm was proposed by Chen et al. [4]. Guo et al. [5,6] proposed a hierarchical linkage based algorithm for

* Tel.: +90 212 285 3590.
  E-mail address: kamasak@gmail.com.

clustering pixels. Brankov et al. [7] defined a new distance metric for pixel TACs and used this metric for clustering. Automatic clustering can either be integrated into [8] or performed simultaneously [9] with kinetic parameter estimation algorithms. In some studies, segmentation is used to estimate the plasma input function from the PET images without arterial sampling [10,11].

The image-domain algorithms require tomographic reconstructions of emission images. TACs extracted from the emission images are used as features for clustering. Recently, we proposed an algorithm that clusters dynamic PET images directly on the sinogram domain [1]. Simulations showed that the algorithm that was proposed in that study produced better clustering results and more accurate cluster TACs compared to image-domain algorithms. In [1], the sinograms are assumed to have Poisson distribution. However, if the data are corrected for randoms, deadtime, scatter, and for some other artifacts, the corrected sinograms are not Poisson distributed anymore [12]. There are many distributions that are proposed to model pre-corrected PET data. Some of these models are ordinary Poisson distribution, shifted Poisson distribution, saddle point approximation [13], and Gaussian distribution [14,15]. In this paper, we extend our Poisson distributed sinogram domain clustering algorithm for the Gaussian distributed sinograms. For this purpose, the proposed clustering framework of [1] is adapted for the Gaussian distributed sinograms.

This paper is organized as follows: in Section 2, the mathematical notation is introduced, the framework and formulation are described for the proposed clustering algorithm with Gaussian distributed sinogram data. In Section 3, the existing image-domain clustering algorithms are explained. Using simulations, the proposed method and image-domain methods are compared in Section 4. The conclusions are presented in Section 5.

2. Unsupervised clustering on sinogram domain

In this section the scanner model and the MAP framework for Gaussian distributed sinogram data are briefly introduced.

Assume that the sinogram data are collected at K time frames, and there are L clusters. Each cluster has an associated TAC and a set of pixels that are in the cluster. For cluster l, let $\mu_l = [\mu_{l0}, \ldots, \mu_{l(K-1)}]$ denote the TAC of the cluster, and let Ω_l denote the set of pixels that belong to this cluster. Let μ denote $L \times K$ matrix formed as $\mu = [\mu_0, \mu_1, \ldots, \mu_{L-1}]^T$ where superscript T denotes the matrix transpose. Let Ω denote the label image, i.e. $\Omega = \{\Omega_0, \ldots, \Omega_{L-1}\}$.

The MAP estimates of μ and Ω are

$$(\mu, \Omega) \leftarrow arg \max p(\mu, \Omega|Y), \tag{1}$$

where Y denotes the sinogram measurements and $p(\cdot)$ denotes the probability.

In the following sections, $p(Y|\mu, \Omega)$ is formulated with the assumption of Gaussian distributed sinograms, and iterative estimation of (μ, Ω) is described.

2.1. Scanner model

The sinogram measurement for projection $0 \leq m < M$ at time frame $0 \leq k < K$ is denoted as Y_{mk}. Y is an $M \times K$ sinogram matrix formed by Y_{mk} that are independent Gaussian distributed random variables. The expected number of counts for each measurement at a given time, t_k is given by:

$$E[Y_{mk}|\mu, \Omega] = \sum_{l=0}^{L-1} \sum_{s \in \Omega_l} A_{ms}\mu_{lk}, \tag{2}$$

where A is the forward projection matrix with elements A_{ms}. Furthermore, let's define

$$Q_{ml}(\Omega) = \sum_{s \in \Omega_l} A_{ms}, \tag{3}$$

$$Q_m(\Omega) = [Q_{m0}, \ldots, Q_{m(L-1)}], \tag{4}$$

and

$$Q(\Omega) = \begin{bmatrix} Q_0 \\ \vdots \\ Q_{M-1} \end{bmatrix} \tag{5}$$

Using this notation, Eq. (2) can be expressed as

$$E[Y|\mu, \Omega] = Q(\Omega)\mu. \tag{6}$$

If the sinogram data are Gaussian distributed, the probability density function is

$$p(Y|\mu, \Omega) = \prod_{k=0}^{K-1} \prod_{m=0}^{M-1} \frac{1}{\sqrt{2\pi}\sigma_{mk}} \exp\left\{ \frac{-1}{2\pi\sigma_{mk}^2}(Y_{mk} - Q_m(\Omega)\mu_{*k})^2 \right\} \tag{7}$$

where σ_{mk} is the standard deviation of Y_{mk}.

2.2. Estimation framework

A cost function, i.e.:

$$C(Y|\mu, \Omega) = -ln(p(Y|\mu, \Omega)) + S(\Omega) \tag{8}$$

is formed as in [1] by negating the logarithm of the probability density function given in (7) and adding a regularization function, $S(\Omega)$. The log likelihood term in the cost function has to be derived for Gaussian distributed sinogram measurements. The regularization function is similar to the one that was proposed by Besag [16]. This regularization function penalizes the local label changes and therefore it controls the spatial continuity of pixel labels. The label image is modelled using a Markov random field (MRF) with Gibbs distribution as in [1].

The probability of a label image, Ω is

$$p(\Omega) = \frac{1}{Z} \exp\left\{ -\beta \sum_{s,r \in \mathcal{N}} g_{s-r}(1 - \delta(\omega_s, \omega_r)) \right\}, \tag{9}$$

where Z is the normalization constant, $\mathcal{N}$ is the set of all spatially neighboring pixel pairs in Ω, g_{s-r} is the coefficient linking pixels s and r, β is a constant that controls the spatial smoothness of the label image, and $\delta(\cdot, \cdot)$ denotes the Kronecker delta function. The negative logarithm of (9) is used as the regularization function, i.e.:

$$S(\Omega) = \beta \sum_{s,r \in \mathcal{N}} g_{s-r}(1 - \delta(\omega_s, \omega_r)). \tag{10}$$

High values of the regularization parameter β, will result in smoother label images.

The labels and region TACs are assigned to minimize the cost function given in (8):

$$\Omega, \mu \leftarrow arg \min C(Y|\Omega, \mu). \tag{11}$$

2.3. Clustering with iterative coordinate descent clustering (CICD)

Clustering with iterative coordinate descent (CICD) is an iterative coordinate-descent minimization technique that was proposed in [1]. CICD is used to minimize the cost function in (8). A CICD iteration has two steps: first the cluster TACs are fixed and pixel labels are sequentially updated to minimize the cost function. When all pixel labels are assigned, the cluster TACs are updated to minimize the cost function as the second step. Therefore, the cost monotonically decreases with each CICD iteration.

2.3.1. Pixel label update
Given fixed cluster TACs, pixel labels can be updated sequentially to minimize the cost function given in (8). If we change the label of pixel s from ω_s to $\tilde{\omega}_s$, the change in the cost function is

$$\Delta C(Y|\omega_s, \tilde{\omega}_s) = C(Y|\omega_s) - C(Y|\tilde{\omega}_s) = ln(p(Y|\tilde{\omega}_s)) - ln(p(Y|\omega_s))$$

$$+ \beta \sum_{r \in \partial s} g_{s-r}(1 - \delta(\tilde{\omega}_s, \omega_r)) \tag{12}$$

where

$$ln(p(Y|\tilde{\omega}_s)) - ln(p(Y|\omega_s))$$

$$= \sum_{k=0}^{K-1} \sum_{m=0}^{M-1} \frac{A_{ms}(-2(Y_{mk} - Q_m(\Omega)) + A_{ms}(\mu_{\tilde{\omega}_s k} - \mu_{\omega_s k}))}{\sigma_{mk}^2} \tag{13}$$

and ∂s is the set of pixels that are 8-connected neighbors of pixels s. Since A is a sparse matrix, there will be a few nonzero terms in (13).

The label of each pixel is updated as

$$\tilde{\omega}_s \leftarrow arg \min \Delta C(Y|\omega_s, \tilde{\omega}_s) \tag{14}$$

to minimize the cost function. This minimization is performed by simply searching through all possible L values of $\tilde{w}_s \in \{0, 1, \ldots, w_s, \ldots, (L-1)\}$. $\{Q_{ml}\}_{l=0}^{L-1}$ are stored in the memory, and they are updated with pixel label updates. For example, if the label of pixel s changes from ω_s to $\tilde{\omega}_s$, the values

of $Q_{m\omega_s}$ and $Q_{m\tilde{\omega}_s}$ are updated as follows:

$$\begin{aligned} Q_{m\omega_s} &\leftarrow Q_{m\omega_s} - A_{ms} \\ Q_{m\tilde{\omega}_s} &\leftarrow Q_{m\tilde{\omega}_s} + A_{ms} \quad \text{for} \quad m = 0 \ldots M-1. \end{aligned} \tag{15}$$

2.3.2. Cluster TAC update
The cluster TACs are updated after all pixel labels are assigned. Since the cost function is quadratic in terms of μ, a closed form expression exists for the cluster TAC that minimizes the cost. The first and second derivative of the cost function with respect to μ_{lk} are

$$\frac{d}{d\mu_{lk}} C(Y|\mu) = -2 \sum_{m=0}^{M-1} \frac{Q_{ml}(Y_{mk} - Q_m(\Omega)\mu_{*k})}{\sigma_{mk}^2} \tag{16}$$

and

$$\frac{d^2}{d\mu_{lk}^2} C(Y|\mu) = 2 \sum_{m=0}^{M-1} \frac{Q_{ml}^2}{\sigma_{mk}^2}. \tag{17}$$

The gradient and hessian of the cost function are

$$\nabla_{\mu_l} = \begin{bmatrix} \frac{d}{d\mu_{l0}} C(Y|\mu) \\ \frac{d}{d\mu_{l1}} C(Y|\mu) \\ \vdots \\ \frac{d}{d\mu_{l(K-1)}} C(Y|\mu) \end{bmatrix} \tag{18}$$

$$\nabla_{\mu_l}^2 = \text{diag} \left\{ \frac{d^2}{d\mu_{l0}^2} C(Y|\mu), \frac{d^2}{d\mu_{l1}^2} C(Y|\mu), \ldots, \frac{d^2}{d\mu_{l(K-1)}^2} C(Y|\mu) \right\}. \tag{19}$$

The cluster TAC that minimizes the cost function is computed as

$$\tilde{\mu}_l = \mu_l - (\nabla_{\mu_l}^2)^{-1} \nabla_{\mu_l}. \tag{20}$$

3. Image-domain clustering algorithms

In this section, two of the image-domain clustering algorithms; weighted least squares clustering and Gaussian mixture model with expectation maximization methods are briefly described. These algorithms require tomographic reconstruction of emission images. In this section, x_{sk} denotes the reconstructed emission rate for pixel s at time frame k, and $x_s = [x_{s0}, \ldots, x_{s(K-1)}]$ is the reconstructed time response of pixel s.

3.1. Weighted least squares clustering (WLS)

The weighted least squares clustering (WLS) is a distance-based clustering algorithm that was proposed by Wong et al. [3]. In this algorithm, the weighted square distance between

the pixel TACs and the cluster TACs are minimized, i.e.:

$$(\mu, \Omega) \leftarrow \underset{\mu, \Omega}{arg\min} \sum_{l=0}^{L-1} \sum_{s \in \Omega_l} \|x_s - \mu_l\|_W^2, \qquad (21)$$

where W is a weight matrix, and $\|x\|_W^2$ denotes $x^T W x$. The diagonal weighting matrix is formed as $W = \text{diag}\{\Delta t_k\}_{k=0}^{K-1}$ where Δt_k is the duration of k th time frame.

This algorithm also updates the pixel labels and cluster TACs iteratively. Each iteration has two steps: in the first step, labels of pixels are sequentially updated. The label of a pixel is updated as follows:

$$\tilde{\omega}_s \leftarrow \underset{l}{arg\min} \|x_s - \mu_l\|_W^2 \qquad (22)$$

After all pixel labels are assigned, the cluster TACs are updated as follows to decrease the weighted distance given in (21):

$$\mu_l = \frac{1}{|\Omega_l|} \sum_{s \in \Omega_l} x_s, \qquad (23)$$

where $|\Omega_l|$ denotes the number of pixels that are labeled as l. The cost function monotonically decreases with each WLS iteration. The iterations are repeated until the stopping (convergence) criterion is reached.

3.2. Gaussian mixture model with expectation maximization (GMM-EM)

In Gaussian mixture model with expectation maximization (GMM-EM) method, the pixel TACs are assumed as samples from Gaussian mixtures that correspond to clusters with different TACs. In this method, pixel labels and cluster TACs are updated iteratively.

Let R_l denote the covariance matrix, and π_l denote the prior probability of cluster l. The posterior probability of a pixel being in cluster l is

$$p(\omega_s = l | x_s, \mu_l) = \frac{\pi_l}{(2\pi)^{K/2}} |R_l|^{-1/2} \exp\left\{ -\frac{1}{2}(x_s - \mu_l)^T R_l^{-1}(x_s - \mu_l) \right\}. \qquad (24)$$

Using the TACs and covariance matrices of the clusters computed from the previous iteration, pixel labels are assigned to maximize the posterior, i.e.:

$$\omega_s \leftarrow \underset{l}{arg\min} \left\{ \frac{1}{2}(x_s - \mu_l)^T R_l^{-1}(x_s - \mu_l) + \frac{1}{2} \log|R_l| - \log(\pi_l) \right\}. \qquad (25)$$

Once the labels are assigned, the cluster TACs and covariance matrices are updated using the EM algorithm [17].

4. Simulations

The proposed clustering algorithm is tested on two different simulated datasets. Emission images at different times are generated using a phantom and kinetic parameters for the 2-tissue compartment model. Both the phantom and kinetic

Fig. 1 – Single slice NCAT phantom that is used in the simulations.

model parameters for the datasets are obtained from the literature.

Emission images are then forward projected into sinogram frames of 180 angles and 200 projections. The plasma function, $C_P(t)$, is taken from Wong et al. [18]. Total scan time is 60 min., which is divided into 18 time frames: 4×0.5 min, 4×2 min, and 10×5 min. The phantom resolution is 128×128 for both datasets. The data are not decay-corrected.

4.1. NCAT dataset

The phantom is taken from NURBS based Cardiac-Torso Phantom (NCAT) dataset [19]. The phantom that is shown in Fig. 1 consists of three distinct regions; background, liver, and tumor. The kinetic parameters of the background, liver and tumor are taken from [20,21]. The TACs of the regions are shown in Fig. 2. The tracer is assumed to be fluoro-deoxy-glucose (FDG) labeled with ^{18}F, which has a decay constant of $\lambda = 0.0063 \, \text{min}^{-1}$. The NCAT dataset is used for simulation of Gaussian distributed and pre-corrected sinogram data.

4.2. Rat dataset

Rat dataset is taken from Kamasak et al. [22]. It is a rat head whose regions are shown in Fig. 3. It has six separate regions including the background. The regional TACs are shown in
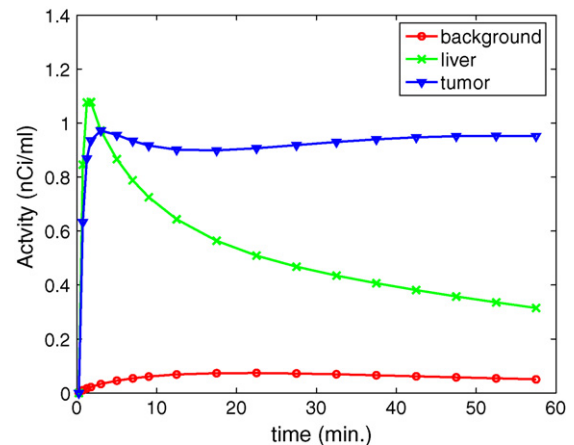
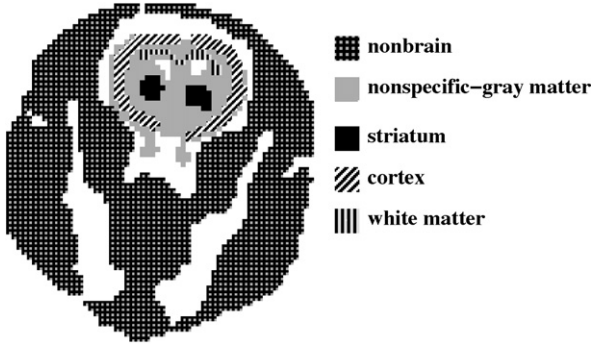**Fig. 2 – Simulated time activity curves corresponding to background, liver, and tumor regions in the NCAT phantom.**

Fig. 3 – Single slice rat phantom that is used in the simulations.

Fig. 4. Poisson noise is used with this dataset. For further details about this phantom see Kamasak et al. [22].

4.3.   Performance evaluation

Dice similarity coefficient (DSC), Kappa statistics, and RMSE of the cluster TACs are used as measures of clustering performance. Dice similarity coefficient is computed as

$$DSC = \frac{\sum_{s=1}^{N} \delta(\omega_s^{estimated}, \omega_s^{original})}{N}. \tag{26}$$

Kappa statistic is computed as

$$\kappa = \frac{P_o - P_c}{1 - P_c} \tag{27}$$

where

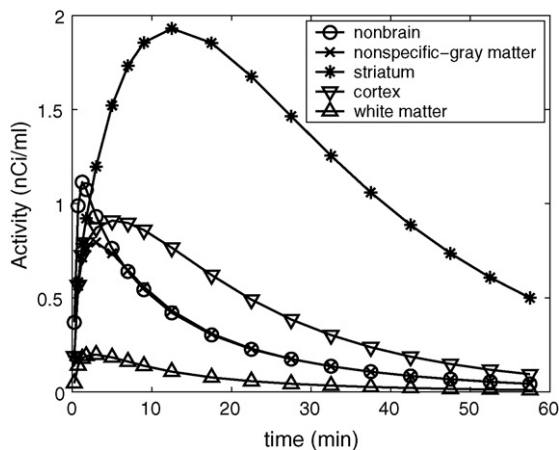$$P_o = \frac{\sum_{s=1}^{N} \delta(\omega_s^{estimated}, \omega_s^{original})}{N}, \tag{28}$$

Fig. 4 – Simulated time activity curves for 5 distinct tissue regions in the rat phantom.

Table 1 – DSC and κ statistics for the Gaussian distributed sinogram of NCAT dataset.		
Method	DSC	κ
ICD + WLS	0.984	0.963
ICD + GMM	0.962	0.913
CICD-Gaussian	0.998	0.995
CICD-Poisson	0.993	0.985

and

$$P_c = \sum_{l=1}^{L} \frac{\sum_{s=1}^{N} \delta(\omega_s^{estimated}, l)}{N} \frac{\sum_{s=1}^{N} \delta(\omega_s^{original}, l)}{N}. \tag{29}$$

In (26), (28), and (29); N denotes the total number of pixels, $\omega_s^{estimated}$ denotes the label of pixel s assigned by the clustering algorithm, and $\omega_s^{original}$ denotes the correct label of pixel s. DSC and κ can take values between zero and one. Higher DSC and κ values correspond to better clustering results.

The RMSE, given in (30), is used to evaluate the accuracy of the estimated cluster TACs. The RMSE of the TAC estimations is computed as

$$RMSE = \sqrt{\frac{1}{K} \sum_{l=1}^{L} \|\mu_l^{estimated} - \mu_l^{original}\|^2}, \tag{30}$$

where $\mu_l^{estimated}$ denotes the estimated TAC for cluster l, and $\mu_l^{original}$ is the correct TAC for cluster l.

4.4.   Simulation results

The image-domain clustering algorithms require the emission images for each time frame. Iterated coordinate descent (ICD) algorithm is used to obtain the required reconstructions [23]. A quadratic prior with different regularization parameters for each time frame is used with ICD. The regularization parameters are chosen to minimize the RMSE of the emission images.

Initial pixel labels and cluster TACs are same for the CICD and image-domain clustering algorithms. Initialization process is described at [1].

All algorithms are stopped when none of the pixels change label during an iteration.

4.4.1.   Results for Gaussian distributed sinograms of NCAT dataset

The images are clustered into four regions that are shown in Fig. 1. For these simulations, the regularization parameters β, for both CICD-Gaussian and CICD-Poisson algorithms are set to 40. This value for β is chosen empirically to maximize the DSC. The pixel labels that are assigned by the image-domain algorithms and the CICD methods are shown in Fig. 5. DSC and κ statistics for these clustering results are listed in Table 1. The CICD methods have higher DSC and κ values than image-domain clustering algorithms. In addition, CICD-Gaussian algorithm has slightly higher DSC and κ values than CICD-Poisson algorithm.
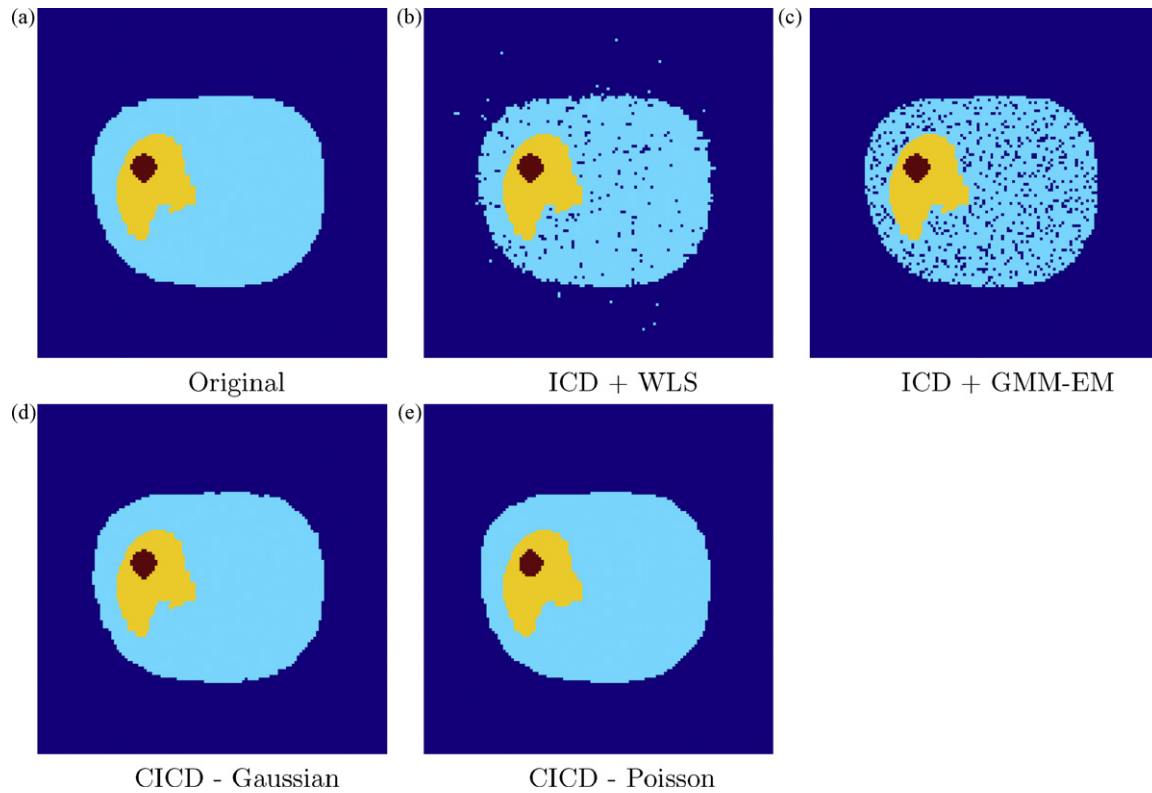
Fig. 5 – Pixel labels assigned to the Gaussian distributed sinogram of NCAT dataset. (a) Original, (b) ICD + WLS, (c) ICD + GMM − EM, (d) CICD-Gaussian, (e) CICD-Poisson.
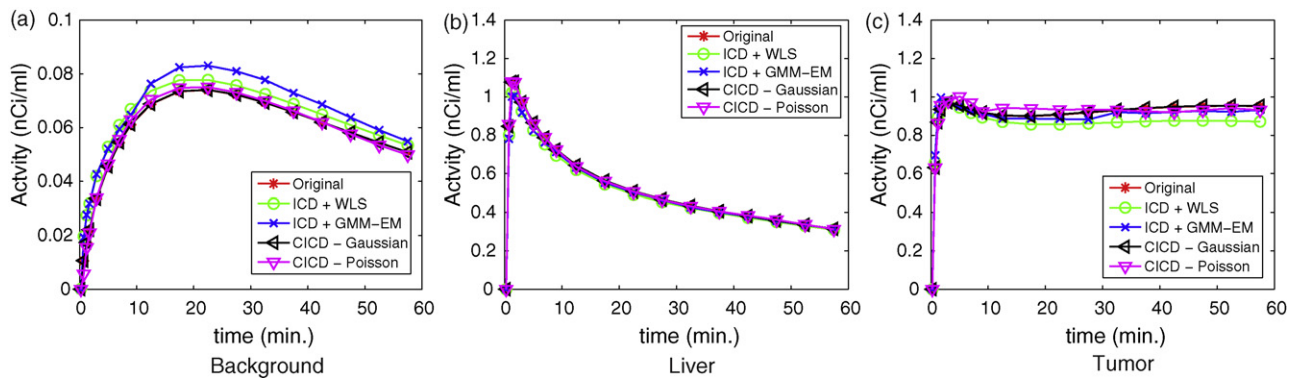

Fig. 6 – Cluster TACs for the Gaussian distributed sinogram of NCAT dataset. (a) Background, (b) liver, (c) tumor.

The RMSE values of the estimated cluster TACs are shown in Fig. 6, and the corresponding RMSE values are given in Table 2. For all regions, CICD-Gaussian algorithm produced the lowest RMSE for cluster TACs.

Clustering results of the CICD-Gaussian algorithm with different β values are shown in Fig. 7. DSC and κ statistics of the clustering results for different values of β are illustrated in Fig. 8.

4.4.2. Results for Poisson distributed sinogram data of rat dataset

The images are clustered into six regions that are shown in Fig. 3. For these simulations, the regularization parameter, β, is set to 50 for for both CICD-Gaussian and CICD-Poisson algorithms, which is chosen to maximize the DSC.

Clustering results of the image-domain algorithms and the CICD algorithms are shown in Fig. 9. The DSC and κ statistics

Region	WLS	GMM-EM	CICD-Gaussian	CICD-Poisson
Table 2 – RMSE of the cluster TACs for the Gaussian distributed sinogram of NCAT dataset.				
Background	0.0123	0.0157	0.0002	0.0033
Liver	0.0626	0.0721	0.0007	0.0088
Tumor	0.1042	0.0664	0.0029	0.0501
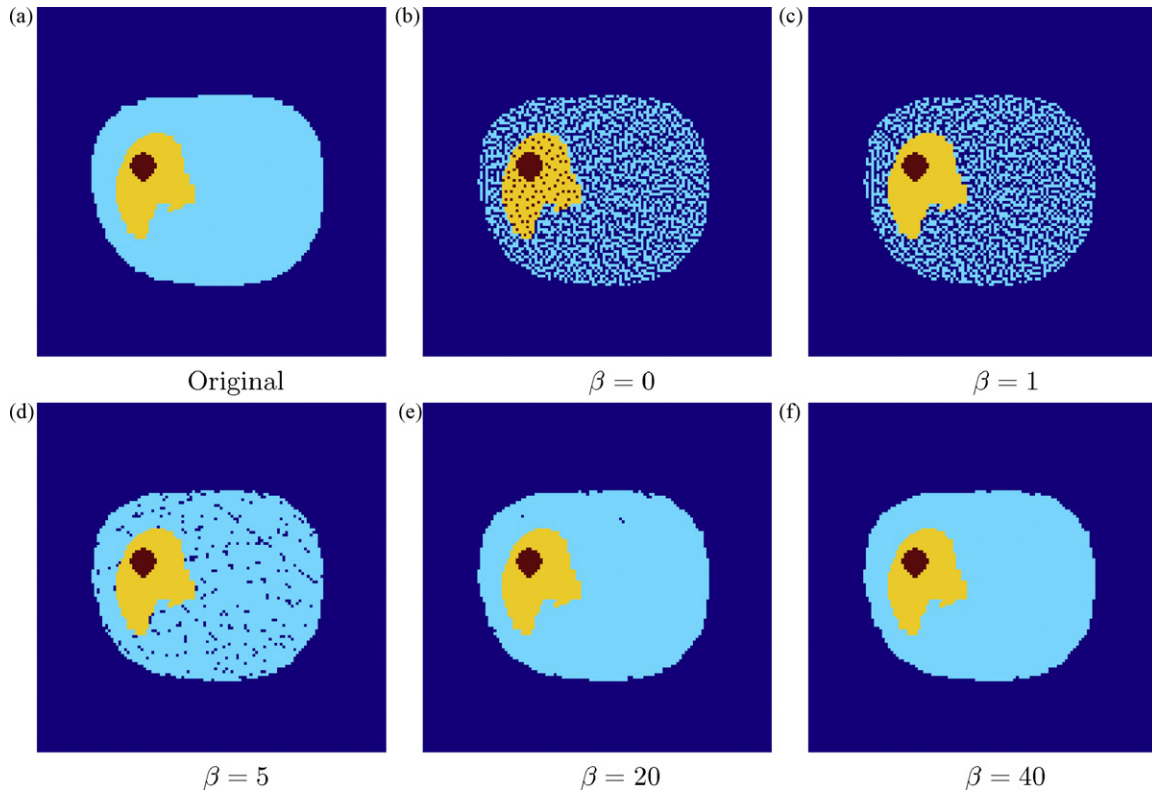
Fig. 7 – Clustering results of CICD-Gaussian algorithm for the Gaussian distributed sinogram of NCAT dataset using different values of β. (a) Original, (b) β = 0, (c) β = 1, (d) β = 5, (e) β = 20, (f) β = 40.

for these algorithms are given in Table 3. From Fig. 9 and Table 3, it can be seen that CICD methods performs better clustering in terms of DSC and κ statistics. Clustering results with CICD-Poisson algorithm have higher DSC and κ statistics compared to the results of CICD-Gaussian algorithm.

TACs estimated by the clustering algorithms are shown in Fig. 10. The RMSE for the estimated cluster TACs are listed in Table 4. For all regions except the white matter, the CICD algorithms estimated the lowest RMSE TACs. TACs estimated by the CICD-Poisson algorithm have lower RMSE compared to the estimates of the CICD-Gaussian algorithm for all regions in the rat dataset.

4.4.3. Results for pre-corrected sinogram data of NCAT dataset

The CICD algorithms: CICD-Gaussian and CICD-Poisson are compared against each other using pre-corrected sinogram simulation of the NCAT dataset. Effects of scatter, randoms, attenuation, deadtime, and detector efficiency are simulated using NCAT dataset. The data are corrected before clustering with CICD algorithms. Simulations are performed with 15% scatter (to count) fraction and 30% scatter fraction. Typically, 10–20% scatter fraction occurs when a septa is used to acquire 2D PET data. Without septa, 3D PET data are acquired with 20–40% scatter fraction.
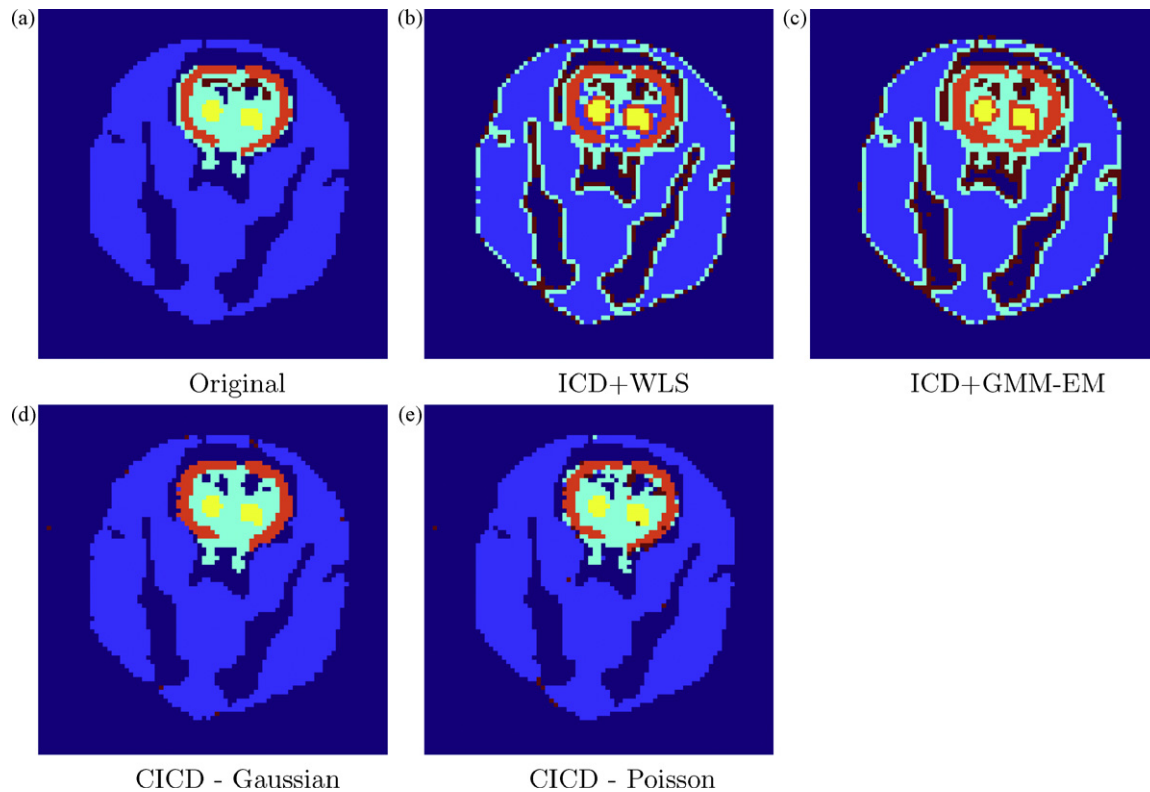
Pixel labels assigned by the CICD-Gaussian and CICD-Poisson algorithms for the pre-corrected sinogram data are shown in Fig. 11. DSC and κ statistics for these labels are listed in Table 5. These results show that the CICD-Gaussian algorithm performs better than the CICD-Poisson algorithm for the pre-corrected data with both 15% and 30% scatter fractions.

Fig. 8 – DSC and κ statistics of the CICD-Gaussian clustering results with different β values.

Table 3 – DSC and κ statistics for the Poisson distributed sinogram of rat dataset.		
Method	DSC	κ
ICD + WLS	0.946	0.814
ICD + GMM	0.938	0.798
CICD-Gaussian	0.993	0.974
CICD-Poisson	0.996	0.983

Table 4 – RMSE of the cluster TACs for the Poisson distributed sinogram of rat dataset.

Region	WLS	GMM-EM	CICD-Gaussian	CICD-Poisson
Background	0.017	0.022	0.000	0.0000
Nonbrain	0.013	0.007	0.013	0.0004
Nonspecific-gray matter	0.088	0.092	0.022	0.0063
Striatum	0.207	0.239	0.033	0.0218
Cortex	0.059	0.088	0.025	0.0110
White matter	0.059	0.019	0.838	0.2167

Fig. 9 – Pixel labels assigned to the Poisson distributed sinogram of rat dataset. (a) Original, (b) ICD + WLS, (c) ICD+GMM-EM, (d) CICD-Gaussian, (e) CICD- Poisson.

The performance of the CICD clustering algorithms are lower on the pre-corrected sinogram data compared to Gaussian distributed sinogram of NCAT dataset. The CICD-Gaussian algorithm outperforms the CICD-Poisson algorithm for both scatter fractions of the pre-corrected sinogram.

Cluster centers of the pre-corrected sinogram of NCAT dataset that are estimated by the CICD clustering algorithm are shown in Fig. 12. The corresponding RMSE values of the estimated cluster centers are listed in Table 6. The RMSE values of the cluster centers for pre-corrected sinogram data are higher than the RMSE of Gaussian distributed sinogram of the NCAT dataset. In addition, RMSE of cluster TACs increases with scatter fraction in the pre-corrected sinogram data. Estimated cluster centers by the CICD-Gaussian algorithm have lower RMSE compared to the CICD-Poisson algorithm for the pre-corrected sinogram data with both 15% and 30% scatter fraction.

4.4.4. Discussion

The success of the CICD algorithms is due to the reduction in the number of estimated parameters. The CICD algorithms assign N labels and estimates $L \times K$ time points for cluster TACs. However, the image-domain clustering algorithms require the estimation of additional $N \times K$ pixels of emission images.

The results of the CICD-Gaussian method for the Gaussian distributed sinogram of NCAT dataset are better than those of CICD-Poisson algorithm in terms of the DSC, κ statistics, and RMSE criteria. On the other hand, for the Poisson distributed sinogram of the rat dataset, the CICD-Poisson algorithm out-

**Table 5 – DSC and κ statistics for the pre-corrected sinogram of NCAT dataset.**

	15% scatter		30% scatter	
	DSC	κ	DSC	κ
CICD-Gaussian	0.996	0.991	0.993	0.985
CICD-Poisson	0.9912	0.980	0.989	0.976

Table 6 – RMSE of the cluster TACs for the pre-corrected sinogram of NCAT dataset.

	CICD-Gaussian		CICD-Poisson	
	15% scatter	30% scatter	15% scatter	30% scatter
Background	0.0005	0.0013	0.0083	0.0108
Liver	0.0012	0.0022	0.0104	0.0148
Tumor	0.0040	0.0056	0.0560	0.0583
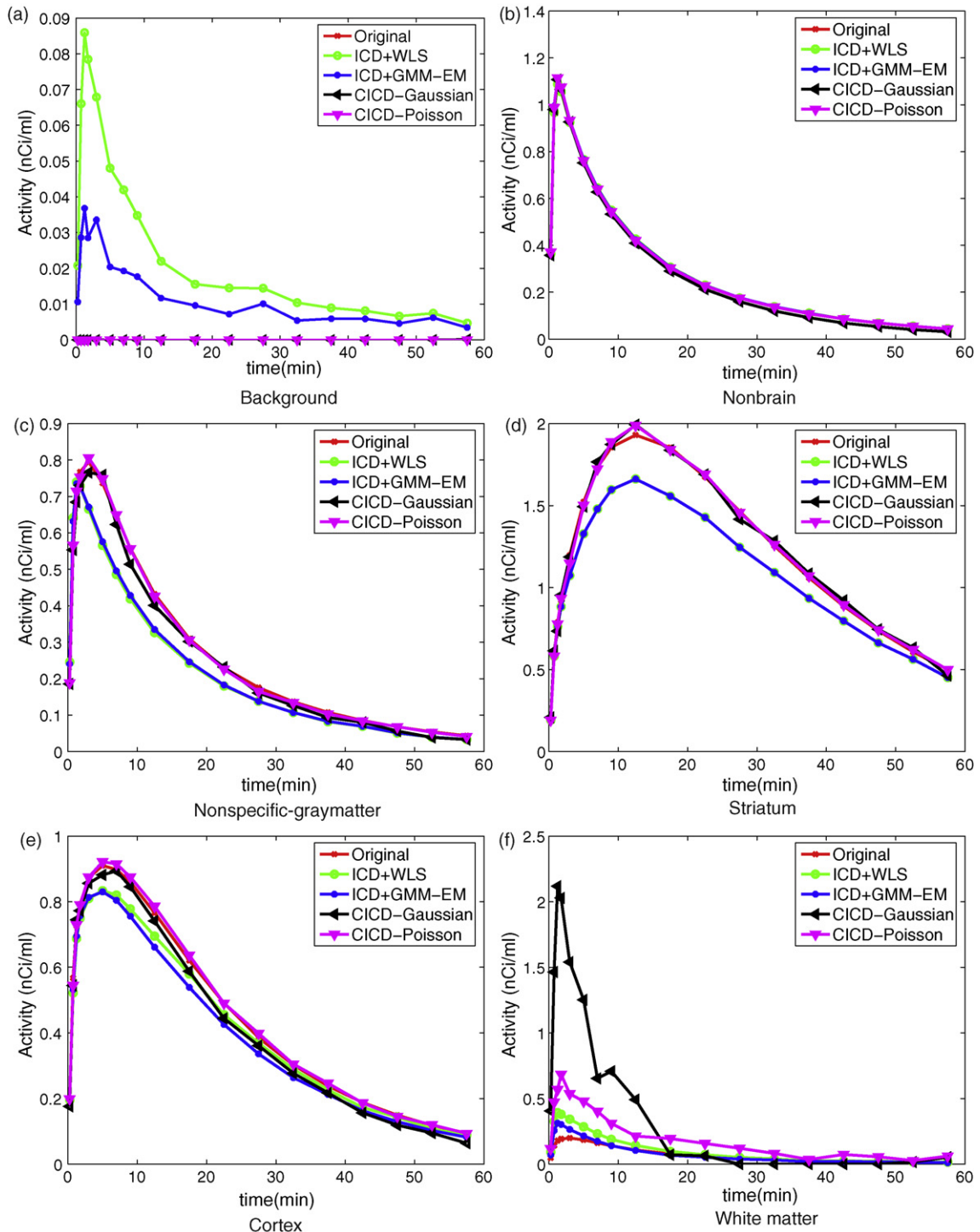
Fig. 10 – Cluster TACs estimated for the Poisson distributed sinogram of rat dataset. (a) Background, (b) nonbrain, (c) nonspecific-gray matter, (d) striatum, (e) cortex, (f) white matter.
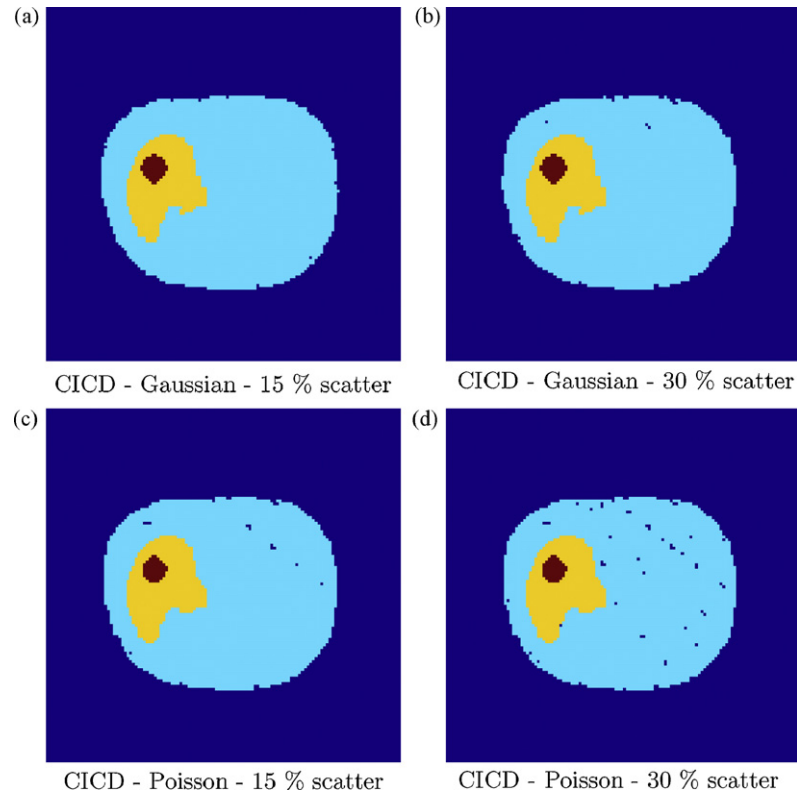
Fig. 11 – Pixel labels assigned to the pre-corrected sinogram of NCAT dataset. (a) CICD-Gaussian – 15% scatter, (b) CICD-Gaussian – 30% scatter, (c) CICD-Poisson – 15% scatter, (d) CICD-Poisson – 30% scatter.
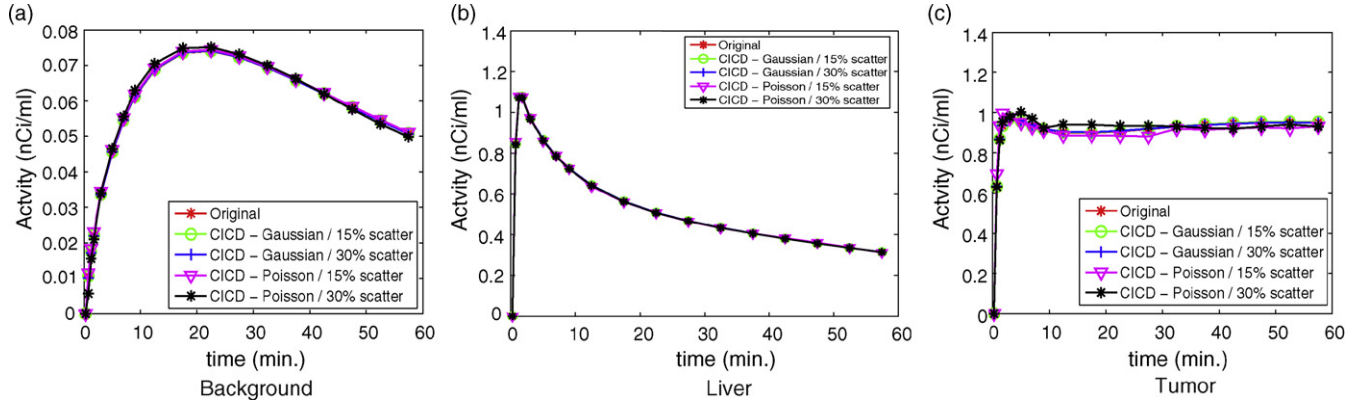
Fig. 12 – Cluster TACs for the pre-corrected sinogram of NCAT dataset. (a) Background, (b) liver, (c) tumor.

performs the CICD-Gaussian algorithm. It can be concluded that the choice of the distribution model for the sinogram data is critical for the performance of the CICD algorithm.

The strength of the regularization term is adjusted with the regularization parameter, β. The regularization parameter, which is chosen to maximize the overall DSC, can make the regularization too strong for small-area regions such as the white matter in the rat dataset. Therefore, the CICD algorithms fail to estimate the TAC of the white matter region. To avoid this, a spatially adaptive regularization scheme can be used.

Both CICD-Gaussian and CICD-Poisson algorithms perform worse on the pre-corrected sinogram data than the Gaussian distributed sinogram of NCAT dataset. This result shows that neither Gaussian nor Poisson distribution can model

the pre-corrected sinogram well enough. On the other hand, the CICD-Gaussian algorithm performs better on the pre-corrected sinograms compared to the CICD-Poisson algorithm. Therefore, it can be concluded that the Gaussian distribution can model the pre-corrected sinogram data better than the Poisson distribution.

5. Conclusion

We recently proposed a new clustering algorithm that we call clustering with iterative coordinate descent [1]. The CICD algorithm clusters the dynamic PET images directly on the projection domain, assigns pixel labels without reconstructing emission images, and estimates the TAC for each cluster.

The CICD algorithm performs better clustering compared to the image-domain clustering algorithms in terms of DSC, κ statistics, and RMSE.

In this paper, the CICD algorithm is extended for the case where the sinogram data are Gaussian distributed. Gaussian distribution can be useful to model sinograms obtained from some of the modern PET systems and sinograms that are pre-corrected. The choice of the data model affects the clustering results. CICD-Gaussian algorithm performs better for the Gaussian distributed sinogram data, whereas the CICD-Poisson algorithm performs better for the Poisson distributed sinogram data. Neither of these distributions may model the pre-corrected data perfectly. However, CICD-Gaussian algorithm performs better than the CICD-Poisson algorithm on the pre-corrected sinogram data.

The proposed clustering method has certain limitations. For example, it is possible to register the emission image frames to compensate inter-frame patient motion in the image-domain clustering algorithms. For the CICD algorithms, the inter-frame patient motion can be recorded during data acquisition using external measurement devices, and the data can be corrected before clustering [24]. In addition, it is sometimes desired to analyze the clustering error corresponding to each pixel. This analysis can give an idea about the accuracy of the pixel labels. With image-domain clustering algorithms, pixel-based error analysis can be performed by comparing the measured TAC of a pixel and the estimated TAC of the corresponding cluster. However, when the pixel labels are assigned directly from the sinograms, this type of error analysis is not straight forward.

REFERENCES

[1] M.E. Kamasak, B. Bayraktar, Clustering dynamic PET images on the projection domain, IEEE Trans. Nucl. Sci. 54 (3) (June 2007) 496–503.

[2] J. Ashburner, J. Haslam, V.J.C.C. Taylor, T. Jones, A cluster analysis approach for the characterization of dynamic PET data, in: R. Myers, V. Cunningham, D. Bailey, T. Jones (Eds.), Quantification of Brain Function Using PET, Academic Press, San Diego, 1996, pp. 301–306.

[3] K.-P. Wong, D. Feng, S.R. Meikle, M.J. Fulham, Segmentation of dynamic PET images using cluster analysis, IEEE Trans. Nucl. Sci. 49 (1) (2002) 200–207.

[4] J.L. Chen, S.R. Gunn, M.S. Nixon, R.N. Gunn, Markov random field models for segmentation of PET images, in: Proceedings of Information Processing in Medical Imaging 2082, 2001, pp. 468–474.

[5] H. Guo, R. Renaut, K. Chen, Clustering for three dimensional kinetic PET data, in: Proceedings of IEEE International Conference on Data Mining, Clustering Large Data Sets, Workshop notes, Melbourne, Florida, 2003, pp. 43–48.

[6] H. Guo, R. Renaut, K. Chen, E. Reiman, Clustering huge data sets for parametric pet imaging, Biosystems 71 (1–2) (2003) 81–92.

[7] J.G. Brankov, N.P. Galatsanos, Y. Yang, M.N. Wernick, Segmentation of dynamic PET or fMRI images based on a similarity metric, IEEE Trans. Nucl. Sci. 50 (5) (2003) 1410–1414.

[8] M.S.Y. Kimura, N. Alpert, Fast formation of statistically reliable FDG parametric images based on clustering and principal components, Phys. Med. Biol. 47 (August 2002) 455–468.

[9] A. Saad, B. Smith, G. Hamarneh, T. Moller, Simultaneous segmentation, kinetic parameter estimation, and uncertainty visualization of dynamic PET images, in: Proceedings of International Conference on Medical Image Computing and Computer Assisted Intervention, Brisbane, Australia, October 29–November 2, 2007.

[10] M. Liptrot, K.H. Adams, L. Martiny, L.H. Pinborg, M.N. Lonsdale, N.V. Olsen, S. Holm, C. Svarer, G.M. Knudsen, Cluster analysis in kinetic modelling of the brain: a noninvasive alternative to arterial sampling, NeuroImage 21 (2) (2004) 483–493.

[11] K.-P. Wong, D. Feng, S.R. Meikle, M.J. Fulham, Non-invasive extraction of physiological parameters in quantitative PET studies using simultaneous estimation and cluster analysis, in: Proceedings of IEEE Medical Imaging Conference, Lyon, France, October 2000, pp. 141–145.

[12] M.N. Wernick, J.N. Aarsvold (Eds.), Emission Tomography: The Engineering and Physics of PET and SPECT, Academic Press, San Diego, 2004.

[13] S. Ahn, J.A. Fessler, Emission image reconstruction for randoms-precorrected pet allowing negative sinogram values, IEEE Trans. Med. Imag. 23 (5) (May 2004) 591–601.

[14] A. Alessio, P. Kinahan, Pet image reconstruction, in: R.E. Henkin (Ed.), Nuclear Medicine, 2nd ed., Mosby, 2006.

[15] M. Yavuz, J.A. Fessler, New statistical models for randoms-precorrected PET scans, in: Information Processing in Medical Imaging, 1997, pp. 190–203.

[16] J. Besag, On the statistical analysis of dirty pictures, J. R. Stat. Soc. B 48 (3) (1986) 259–302.

[17] A.P. Dempster, N.M. Laird, D.B. Rubin, Maximum likelihood from incomplete data via the EM algorithm, J. R. Stat. Soc. B 39 (1) (1977) 1–38.

[18] K.-P. Wong, D. Feng, S.R. Meikle, M.J. Fulham, Simultaneous estimation of physiological parameters and the input function—in vivo PET data, IEEE Trans. Inform. Technol. Biomed. 5 (1) (March 2001) 67–76.

[19] W.P. Segars, Development and application of the new dynamic nurbs-based cardiac-torso (NCAT) phantom, Ph.D. dissertation, The University of North Carolina, 2001.

[20] O.L. Munk, L. Bass, K. Roelsgaard, D. Bender, S.B. Hansen, S. Keiding, Liver kinetics of glucose analogs measured in pigs by PET: importance of dual-input blood sampling, J. Nucl. Med. 42 (2001) 795–801.

[21] A. D-Strauss, L.G. Strauss, C. Burger, A. Ruhl, G. Irngartinger, W. Stremmel, J. Rudi, Prognostic aspects of 18F-FDG PET kinetics in patients with metastatic colorectal carcinoma receiving FOLFOX chemotherapy, J. Nucl. Med. 45 (2004) 1480–1487.

[22] M.E. Kamasak, C.A. Bouman, E.D. Morris, K. Sauer, Direct reconstruction of kinetic parameter images from dynamic PET data, IEEE Trans. Med. Imag. 24 (5) (May 2005) 636–650.

[23] C.A. Bouman, K. Sauer, A unified approach to statistical tomography using coordinate descent optimization, IEEE Trans. Image Process. 5 (3) (March 1996) 480–492.

[24] P.M. Bloomfield, T.J. Spinks, J. Reed, L. Schnorr, A.M. Westrip, L. Livieratos, R. Fulton, T. Jones, The design and implementation of a motion correction scheme for neurological PET, Phys. Med. Biol. 48 (8) (2003) 959–978.